Search for $K_L \to \pi^0\pi^0\gamma\gamma$ and $K_L \to \pi^0\pi^0 X$ where $X \to \gamma\gamma$ at the KOTO Experiment

J. Redeker,[1] C. Lin,[2] Y. W. Wah,[1] J. K. Ahn,[3] M. Gonzalez,[4,*] K. Hanai,[4] Y. B. Hsiung,[5] T. Kato,[4] E. J. Kim,[6] T. K. Komatsubara,[7,8] K. Kotera,[4] S. K. Lee,[6] G. Y. Lim,[7,8] T. Matsumura,[9] H. Nanjo,[4] T. Nomura,[7,8] T. Nunes,[4] K. Ono,[4] K. Shiomi,[7,8] R. Shiraishi,[7] Y. Tajima,[10] Y. C. Tung,[11] H. Watanabe,[7,8] T. Wu,[5] T. Yamanaka,[4] and H. Y. Yoshida[10]

[1]*Enrico Fermi Institute, University of Chicago, Chicago, Illinois 60637, USA*
[2]*Department of Physics, National Changhua University of Education, Changhua 50007, Taiwan*
[3]*Department of Physics, Korea University, Seoul 02841, Republic of Korea*
[4]*Department of Physics, Osaka University, Toyonaka, Osaka 560-0043, Japan*
[5]*Department of Physics, National Taiwan University, Taipei 10617, Taiwan, Republic of China*
[6]*Division of Science Education, Jeonbuk National University, Jeonju 54896, Republic of Korea*
[7]*Institute of Particle and Nuclear Studies, High Energy Accelerator Research Organization (KEK), Tsukuba, Ibaraki 305-0801, Japan*
[8]*J-PARC Center, Tokai, Ibaraki 319-1195, Japan*
[9]*Department of Applied Physics, National Defense Academy, Kanagawa 239-8686, Japan*
[10]*Department of Physics, Yamagata University, Yamagata 990-8560, Japan*
[11]*Department of Physics, National Kaohsiung Normal University, Kaohsiung 824, Taiwan*

(Received 22 March 2026; revised 20 May 2026; accepted 23 June 2026; published 29 July 2026)

We performed searches for $K_L \to \pi^0\pi^0 X$ where X may be an axionlike particle that promptly decays to two photons, and the first search for $K_L \to \pi^0\pi^0\gamma\gamma$ at the KOTO experiment using data taken in 2021. The search is performed for X mass in the range of 160–220 MeV/c^2. Three events were observed in the signal region, with two events near an X mass of 177 MeV/c^2. This result led to a range of upper limits on the branching ratio, $\mathrm{BR}(K_L \to \pi^0\pi^0 X) < (1-20) \times 10^{-7}$ at the 95% confidence level (CL). No events were observed for the analysis of $K_L \to \pi^0\pi^0\gamma\gamma$, setting an upper limit on the branching ratio, $\mathrm{BR}(K_L \to \pi^0\pi^0\gamma\gamma) < 1.69 \times 10^{-6}$ at the 95% CL.

DOI: 10.1103/pt2h-99by

Introduction—Searching for dark sector particles is one of the major tasks in particle physics today. There is theoretical interest in dark particle candidates that couple to quarks in an energy range that a neutral-kaon experiment is sensitive to through the study of rare decays [1–4]. A promising search is the decay $K_L \to \pi^0\pi^0 X$, where X may be an axionlike particle (ALP) that decays promptly. In particular, there are theoretical scenarios that prefer three-body decay modes such as $K_L \to \pi^0\pi^0 X$ over $K_L \to \pi^0 X$ [5,6]. This decay may be observable if X decays to two photons via a quark loop, and if X has a mass different from the π^0. $K_L \to \pi^0\pi^0 X$ was studied in the E391a experiment [7] in a smaller mass range, $M_X \in [194.3, 219.3]$ MeV/c^2. This Letter improves sensitivity up to an order of magnitude in the mass range studied in E391a, while also providing a first search for M_X closer to the π^0 mass. This analysis also provides insight into the rare decay $K_L \to \pi^0\pi^0\gamma\gamma$. This decay is described by chiral perturbation theory (ChPT) [8] up to second order, and a measurement of the branching ratio provides a test of second order ChPT. The branching ratio is within range of the sensitivity of the KOTO experiment at 8.4×10^{-8}, assuming $|M_{\gamma\gamma} - M_{\pi^0}| \geq 10$ MeV/c^2. Additionally, this decay is closely related to the theoretical branching ratio for modes $K_L \to \pi^0\pi^0 l^- l^+$, which were studied in the KTeV experiment [9,10], where the calculation of the branching ratio is fundamentally affected by the process $K_L \to \pi^0\pi^0\gamma^*\gamma^*$, where γ^* is a virtual photon.

The primary purpose of the KOTO experiment at the Japan Proton Accelerator Research Complex (J-PARC) facility in Tokai, Japan, is to search for ultrarare decay $K_L \to \pi^0\nu\bar{\nu}$ [11,12]. KOTO uses the intense 30-GeV proton beam, which is extracted from the main ring toward a gold target in the Hadron Experimental Facility that hosts the KOTO detector. The secondary 20-m neutral beamline is constructed at an angle of 16° off the proton beam axis and collimated with a solid angle of 7.8 μsr, which corresponds to an 8×8 cm^2 beamwidth at the exit of the second collimator [13]. A photon absorber made of 70 mm thick lead was inserted in front of the collimators to reduce

*Present address: CERN, European Organization for Nuclear Research, CH-1211 Geneva, Switzerland.

Published by the American Physical Society under the terms of the Creative Commons Attribution 4.0 International license. Further distribution of this work must maintain attribution to the author(s) and the published article's title, journal citation, and DOI. Funded by SCOAP³.

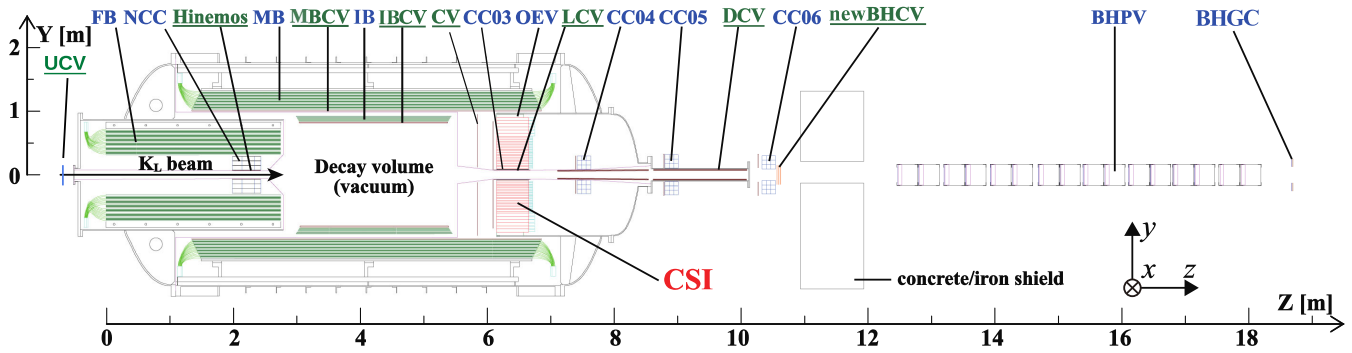


FIG. 1. Cross-sectional side view of the KOTO detector. A detector name with an underline implies it is a charged particle veto counter. All others, except for the CSI calorimeter, are photon veto counters.

the number of photons entering the detector volume. A sweeping magnet was installed between the two collimators to reduce the number of charged particles entering the detector volume. The K_L momentum spectrum peaks at 1.4 GeV/c at the entrance of the detector and was measured during an engineering run in 2012 using the $K_L \to \pi^+\pi^-\pi^0$ decay [14,15]. A cross-sectional schematic of the KOTO detector is shown in Fig. 1. The origin is set on the beam axis and at the upstream side of the front barrel (FB). The calorimeter (CSI) [16] has a diameter of 1.9 m and a depth of 27 radiation lengths. The primary purpose of the calorimeter is to detect photons from K_L decays and measure their position, energy, and timing. The calorimeter consists of an array of 2716 undoped CsI crystals with the dimensions of $2.5 \times 2.5 \times 50$ cm^3 (inner) and $5 \times 5 \times 50$ cm^3 (outer). KOTO uses a hermetic veto system to detect all particles that arise from a K_L decay within the detector region. The largest veto detectors consist of lead plastic-scintillator sandwich counters that enclose the decay volume called the inner barrel, main barrel, and front barrel (IB, MB, and FB) [17,18]. Plastic scintillators to detect charged particles are placed on the inner surface of the IB and MB, as well as in front of CSI, called the inner barrel charged veto, main barrel charged veto, and charged veto (IBCV, MBCV, and CV) [19]. Other veto detectors such as the neutron collar counter (NCC) and collar counters CC03–6 are made with additional undoped CsI crystals that are placed near the beam axis. The beam-hole veto detectors consist of three layers of wire chambers for the detection of charged particles (newBHCV) and an arrangement of aerogel Cherenkov counters with lead converters for the detection of photons (BHPV) [20], called the beam-hole charged veto and beam-hole photon veto, respectively. Other detectors shown in Fig. 1 are not used in this analysis. The data acquisition system relies on two stages of trigger logic [21]. The first trigger stage (L1) required the total deposited energy in CSI to be larger than 550 MeV and no hits in NCC, MB, IB, CV, CC03, CC04, CC05, or CC06 detectors. The second trigger stage (L2) selected events based on the number of clusters of deposit energy in CSI. For the study of $K_L \to \pi^0\pi^0\gamma\gamma$ and $K_L \to \pi^0\pi^0X$, the number of clusters was required to be 6. The same trigger condition was used to study the $K_L \to 3\pi^0$ decay to evaluate the background level and the K_L yield. Once a trigger condition was passed, the digitized waveforms of each channel were recorded for offline analysis.

Event reconstruction—Event reconstruction involves calculating complex analysis variables from the measured waveforms in data. For $K_L \to \pi^0\pi^0\gamma\gamma$, there is no missing information since all final state particles are measured. There are 45 combinations of two photons to pair with the two pions. A constrained fit strategy is used for the reconstruction of $K_L \to \pi^0\pi^0\gamma\gamma$. The energy and hit position of the photons in the CSI should be well reconstructed and follow conservation of momentum and energy constraints. In total, there are five constraints applied in the reconstruction. First, the reconstructed invariant mass of the six photons should be the K_L mass. The second and third constraints require the invariant mass of two of the photon pairs to be the pion mass. Lastly, the fourth and fifth constraints require the K_L momentum vector to lie on the line connecting the gold target and the center of energy on CSI. The constraints are used to modify the reconstruction variables, such as the decay vertex, kaon and pion momentum, and photon hit position and energy, to best fit the constraints. Knowing the position and energy resolution in the calorimeter, the "goodness" of the constrained fit can be quantified in a variable $\chi^2_{\rm fit}$. The $\chi^2_{\rm fit}$ is a function of the photon x, y hit positions on CSI, and the photon energies, and is defined with known resolutions of hit position $(\sigma_{x_i}, \sigma_{y_i})$ and energy (σ_{E_i}) as

$$\chi^2_{\rm fit}(x_1, y_1, E_1, \ldots, x_6, y_6, E_6) = \sum_{i=1}^{6} \frac{(x_i - x_{i,m})^2}{\sigma^2_{x_i}} + \sum_{i=1}^{6} \frac{(y_i - y_{i,m})^2}{\sigma^2_{y_i}} + \sum_{i=1}^{6} \frac{(E_i - E_{i,m})^2}{\sigma^2_{E_i}}. \quad (1)$$

The variables $x_{i,m}, y_{i,m}$, and $E_{i,m}$ represent the initial measured reconstructed position and energy of the photon hit, while x_i, y_i, and E_i are the fitted results obtained by minimizing the $\chi^2_{\rm fit}$ function and are used in the following

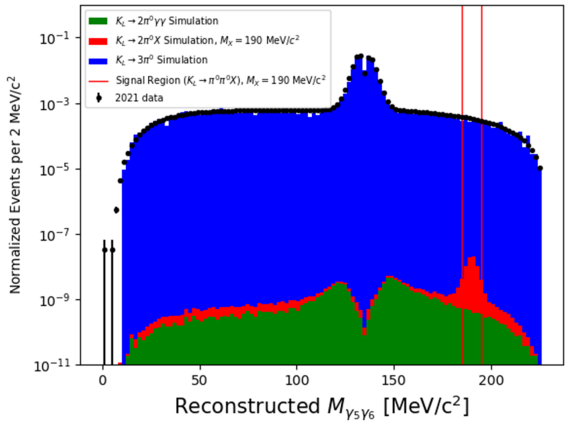


FIG. 2. Invariant mass, $M_{\gamma_5\gamma_6}$, distribution in data, overlaid with the $K_L \to 3\pi^0$ background simulation normalized to the branching ratio. The signal simulation is weighted according to an assumed $\mathrm{BR}(K_L \to \pi^0\pi^0 X) = 1 \times 10^{-7}$ and $\mathrm{BR}(K_L \to \pi^0\pi^0\gamma\gamma) = 8.4 \times 10^{-8}$ [8].

analysis. Out of the 45 possible combinations, the pairing that returns the smallest χ^2_{fit} value was chosen as the best fit for the reconstruction. This χ^2_{fit} was obtained using the signal constraints and will be denoted as $\chi^2_{\mathrm{fit}}(2\pi^0\gamma\gamma)$. This reconstruction strategy can likewise be done assuming the decay $K_L \to 3\pi^0$. In this case, there is an additional pion mass constraint, and the photon pairings that give the smallest χ^2_{fit} with an additional pion mass assumption are recorded $[\chi^2_{\mathrm{fit}}(3\pi^0)]$. If $\chi^2_{\mathrm{fit}}(3\pi^0)$ is small, it is likely a background event from $K_L \to 3\pi^0$, whereas for the signal this value should be large as long as the X mass is dissimilar from the pion mass.

The simulation of the decay $K_L \to \pi^0\pi^0 X$, where X decays to 2γ promptly, was performed assuming a flat phase space. Following the same reconstruction, the signal region is defined by the invariant mass of the two photons not used in the pion reconstruction, called $M_{\gamma_5\gamma_6}$. The data overlaid with the simulated Monte Carlo distributions are shown in Fig. 2 after applying basic selection criteria (cuts) for veto and data quality. The simulation of the decay $K_L \to \pi^0\pi^0\gamma\gamma$ was performed following the phase space defined in [8]. Notably, the invariant mass distribution has a pole near the pion mass, and so a precut is applied in the simulation around the pion mass to require $|M_{\gamma_5\gamma_6} - M_{\pi^0}| \geq 10$ MeV/c^2.

Selection process—General criteria were applied to ensure data quality in this analysis. Six clusters in the CSI with no on-time hits in the veto detectors, shown in Fig. 1, were required. The photon hit position (x, y) in CSI was restricted such that $\max(|x|, |y|) > 150$ mm and $\sqrt{x^2 + y^2} < 850$ mm in order to prevent shower leakage on the edge. An event was rejected if the hit position was in the region $(210\ \mathrm{mm} < x < 260\ \mathrm{mm}) \wedge (100\ \mathrm{mm} < y < 135\ \mathrm{mm})$ to avoid CSI regions more likely to induce energy mismeasurement caused by unstable, low gain PMTs. This region was determined by looking at the reconstructed hit positions of γ_5 and γ_6 with large $\chi^2_{\mathrm{fit}}(3\pi^0)$ values in data. The minimum photon energy was required to be larger than 100 MeV, and the minimum cluster distance was required to be larger than 100 mm in order to ensure the individual clusters are well measured. The total energy deposit in CSI was required to be larger than 650 MeV. The reconstructed K_L transverse momentum should be less than 8 MeV/c to protect against energy mismeasurement. The photon hit timing must be within 1 ns of each other. The cluster shape and channel pulses were required to be consistent with a library of photonlike cluster shapes and waveforms, with the discriminators called CSDDL and FPSD, respectively [22].

Selection optimization—To determine the event selection, 10 times the statistics of $K_L \to 3\pi^0$ in data was simulated. This simulation sample was used to determine the selection criteria for the 13 $K_L \to \pi^0\pi^0 X$ analyses with X masses in 5 MeV intervals ranging from 160–220 MeV/c^2, and for $K_L \to \pi^0\pi^0\gamma\gamma$. The cut optimization focused on the three most important variables in these analyses, $\chi^2_{\mathrm{fit}}(3\pi^0)$, $\chi^2_{\mathrm{fit}}(2\pi^0\gamma\gamma)$, and a deep learning cluster shape discriminator (CSDDL) [22]. CSDDL was originally trained to discriminate between neutron and electromagnetic interactions in CSI. However, this variable is highly effective because the photonuclear interactions in CSI will likewise affect the cluster shape, and energy mismeasurement due to the photonuclear effect is the largest cause of $K_L \to 3\pi^0$ background in this analysis. A three-dimensional grid search was done to test each set of cuts and evaluate them based on a figure of merit (FOM) strategy. A FOM strategy optimizes the potential upper limit (U.L.) result by maximizing a function [23],

$$f(N_{\mathrm{sig}}, N_{\mathrm{bkg}}) = \sqrt{2\ln(Q)}, \tag{2}$$

$$Q = e^{-N_{\mathrm{sig}}}\left(1 + \frac{N_{\mathrm{sig}}}{N_{\mathrm{bkg}}}\right)^{N_{\mathrm{sig}}+N_{\mathrm{bkg}}}, \tag{3}$$

where N_{sig} and N_{bkg} were calculated within the region of interest (ROI) of $M_{\gamma_5\gamma_6}$ and represent the number of signal and background events in the ROI, respectively. N_{sig} was calculated assuming a branching ratio of the signal at 10^{-7}. For the X mass analyses, the ROI was found by applying a Gaussian fit on $M_{\gamma_5\gamma_6}$ to the signal simulation and was defined by $\mu_{\mathrm{fit}} \pm 2\sigma_{\mathrm{fit}}$. For the $K_L \to \pi^0\pi^0\gamma\gamma$ analysis, the ROI was defined by the high mass region $M_{\gamma_5\gamma_6} \in [160, 227.66]$ MeV/c^2. By optimizing the event selection process for each analysis, the signal acceptance can be improved by up to a factor of five for X masses near the 160 MeV/c^2 and 220 MeV/c^2.

Control region analysis—In this Letter, the $M_{\gamma_5\gamma_6}$ region above 155 MeV/c^2 was masked to avoid human bias. Because of this, the region with $M_{\gamma_5\gamma_6}$ below 130 MeV/c^2

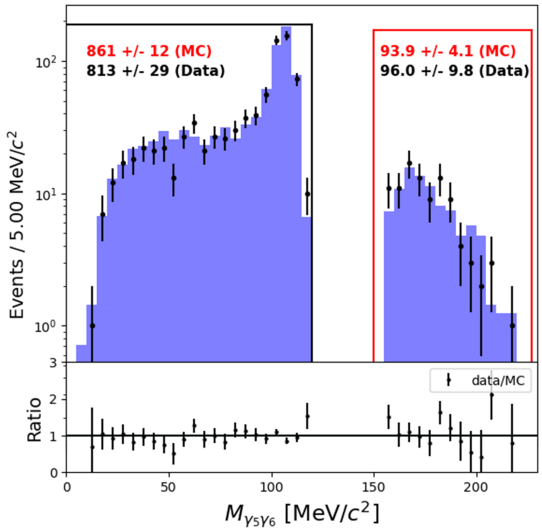


FIG. 3. $K_L \to 3\pi^0$ data (black) and Monte Carlo (blue) comparison after applying the inverse selection and scale factor. The numbers represent the number of data and Monte Carlo events observed in the regions encapsulated by the black (red) lines.

was crucial for understanding the agreement between data and Monte Carlo. If the photonuclear interaction cross section in CSI is larger than predicted by Monte Carlo simulation in KOTO's energy range, we would underestimate $K_L \to 3\pi^0$ background levels. A scale factor may be determined by studying the low mass region after tight selections in data. This factor was simply defined as $F = N_{\rm obs}^{\rm data}/N_{\rm exp}^{\rm MC}$, where $N_{\rm obs}^{\rm data}$ and $N_{\rm exp}^{\rm MC}$ are the number of events observed in data and the number of events expected from Monte Carlo simulation, respectively. Correlations were observed between CSDDL, $\chi^2_{\rm fit}(3\pi^0)$, and F. Since each analysis has different selection criteria, the scale factor, F, was determined independently for each analysis. This factor was typically in the range of 1.5–2.5. The fidelity of this method to evaluate the background level was tested using an inverse selection strategy in the high mass region. Events were required to have $100 < \chi^2_{\rm fit}(3\pi^0) < 115$ to observe the performance at large $\chi^2_{\rm fit}(3\pi^0)$ values while excluding events that may fall in the masked region. All other cut selection criteria are applied except for FPSD. The CSDDL cut was loosened in order to enhance statistics. F was determined using 50% of the $K_L \to 3\pi^0$ Monte Carlo. The agreement between data and Monte Carlo is observed in Fig. 3, tested against 100% of the $K_L \to 3\pi^0$ Monte Carlo.

Single event sensitivity—The set of data analyzed in this article was taken in 2021 with a proton beam intensity between 60–64 kW and corresponds to a total K_L yield at the entrance of the KOTO detector, Y, given by

$$Y = (4.27 \pm 0.03_{\rm stat} \pm 0.31_{\rm sys}) \times 10^{12}. \quad (4)$$

TABLE I. Systematic uncertainties associated with the SES calculation.

Source	Uncertainty (%)
Veto cuts	4.6
Kinematic cuts	2.3
Quality cuts	2.9
K_L momentum	1.5
Trigger	4.1
$\chi^2_{\rm fit}(3\pi^0)$	5 – 8.8
Total	8.9 – 11.5

The yield was determined through the copious $K_L \to 3\pi^0$ decay, then normalized by calculating its acceptance using the Geant4 simulation toolkit [24]. The sensitivity of the analysis result is quantified in the single event sensitivity (SES), which represents the central value of the branching ratio if one signal event is observed and is defined as

$$\mathrm{SES} = \frac{1}{A_{\rm sig} \times Y}. \quad (5)$$

The systematic uncertainty in this calculation is summarized in Table I. The dominant sources of systematic uncertainties are from the veto cut selection (4.6%) and the trigger effect (4.1%). The systematic uncertainties of the veto cut selection, the kinematic cut selection (2.3%), and the χ^2 cut selections (1.7%) were determined by quadratically summing the relative difference in exclusive acceptance between data and Monte Carlo simulation, which is defined as $A_i = N_{\rm all}/N_{\rm all\backslash i}$ where $N_{\rm all}$ and $N_{\rm all\backslash i}$ are the number of events observed after applying all event selections and the number of events observed after applying all but the ith, respectively. The systematic uncertainty from the K_L momentum spectrum is related to the geometrical acceptance, which is the probability to observe all final state particles in CSI, and the kinematic acceptance. The simulated K_L momentum spectrum relies on parameters obtained during engineering runs in 2012 [14,15]. The magnitude of this effect was obtained by calculating the difference in Monte Carlo geometrical acceptance by varying the parameters according to their measured uncertainty. The 1σ variation in the relative difference in acceptance was found to be 1.5%. The systematic uncertainty from the trigger effect was quadratically summed from two sources. The first source is the E_t and veto trigger, which requires the energy deposit in CSI to be larger than 550 MeV and no on-time hits in CV, NCC, CC03–6, and MB or IB detectors, respectively. The second source is the clustering trigger. These triggers may accidentally reject events that would normally be accepted in the offline analysis, and this effect was studied using minimum bias data. These data were taken by requiring at least 400 MeV energy deposit in CSI and no veto or

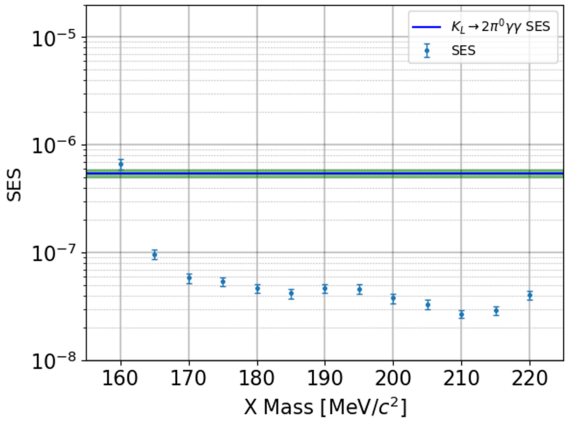


FIG. 4. SES as a function of X mass. The horizontal bar represents the SES of the $K_L \to \pi^0\pi^0\gamma\gamma$ decay. The error bars represent the quadratic sum of the statistical and systematic uncertainty, which is propagated from the K_L yield and A_{sig}.

clustering requirements. The relative difference in acceptance in minimum bias data and after applying the standard trigger condition is quoted as the systematic uncertainty (4.1%). Furthermore, additional systematics were considered in the calculation of the signal acceptance (A_{sig}) since additional selection criteria had been used. The systematic uncertainties were evaluated using $K_L \to 3\pi^0$ data and Monte Carlo as in the K_L yield calculation. The systematic uncertainty in A_{sig} was dominated by $\chi^2_{\text{fit}}(3\pi^0)$ and was between 5 and 8.8%. Other systematics in A_{sig} include the relative difference in exclusive acceptance of data and Monte Carlo for the FPSD (1.7%), CSDDL (0.1%), and $\chi^2_{\text{fit}}(2\pi^0\gamma\gamma)$ (1.6%). The systematic uncertainty labeled "Quality Cuts" represents the quadratic sum of uncertainties associated with $\chi^2_{\text{fit}}(2\pi^0\gamma\gamma)$, FPSD, CSDDL, and the χ^2 selections used to obtain the K_L flux. The total systematic uncertainty in the SES was 8.9–11.5% after quadratically summing all of the sources. The SES varies as a function of X mass, with the details shown in Fig. 4.

Results—The background expectation was dominated by $K_L \to 3\pi^0$ and $K_L \to \pi^0\pi^0\gamma\gamma$ decays, and the level expected for each analysis is shown in Table II. The systematic uncertainty for N_{bkg} is given by the uncertainty in the scale factor F, which was between 9–23%. The results were obtained by opening the signal regions defined by each X mass ROI, while for the $K_L \to \pi^0\pi^0\gamma\gamma$ analysis the entire high mass region was opened at once. Depending on the analysis, $\chi^2_{\text{fit}}(2\pi^0\gamma\gamma) \in [3, 9]$, $\chi^2_{\text{fit}}(3\pi^0) \in [115, 188]$, and the CSDDL threshold was between 0.5 and 0.9. The results are summarized in Table II.

N_{obs} corresponds to the number of events observed in data within the ROI for that specific analysis. The upper limit was determined using the modified frequentist approach and evaluating CL_s [25]. The number of background events is $N_{K_L\to 3\pi^0}$ for the analysis of $K_L \to \pi^0\pi^0\gamma\gamma$, and it is the sum of $N_{K_L\to 3\pi^0}$ and $N_{K_L\to\pi^0\pi^0\gamma\gamma}$ for the analysis of $K_L \to \pi^0\pi^0 X$. The quadratic sum of the uncertainty in N_{bkg} and SES is introduced as nuisance parameters. Across the M_X analyses, the total expected number of $K_L \to 3\pi^0$ background events was $4.49 \pm 0.75_{\text{stat}} \pm 0.73_{\text{sys}}$. The expected number of $K_L \to \pi^0\pi^0\gamma\gamma$ events was $0.65 \pm 0.02_{\text{stat}} \pm 0.07_{\text{sys}}$. Three unique events were observed in the signal regions, which was consistent with our expectation. The event observed in the analysis of $M_X = 175$ MeV/c^2 was also observed in the $M_X = 180$ MeV/c^2 analysis. This was due to overlapping signal regions and the correlation of selection criteria. To account for the correlation between events and provide a clear upper limit distribution, a weighted CL_s was evaluated. Monte Carlo simulation was performed for all integer X

TABLE II. 95% CL upper limits on the branching ratio for each analysis, the number of events observed in data, the expected number of $K_L \to 3\pi^0$ background, and the expected number of $K_L \to \pi^0\pi^0\gamma\gamma$. The mass, M_X, is in units of MeV/c^2.

Analysis	N_{obs}	$N_{K_L\to 3\pi^0}$	$N_{K_L\to\pi^0\pi^0\gamma\gamma}$	BR U.L. ($\times 10^{-7}$)
$M_X = 160$	0	< 0.34 (90% CL)	0.016 ± 0.003	< 20.1
$M_X = 165$	0	0.41 ± 0.22	0.09 ± 0.01	< 2.95
$M_X = 170$	0	0.93 ± 0.35	0.13 ± 0.01	< 1.78
$M_X = 175$	1	0.85 ± 0.35	0.13 ± 0.01	< 2.31
$M_X = 180$	2	0.19 ± 0.14	0.11 ± 0.01	< 2.82
$M_X = 185$	0	< 0.28 (90% CL)	0.056 ± 0.008	< 1.27
$M_X = 190$	0	< 0.38 (90% CL)	0.036 ± 0.006	< 1.42
$M_X = 195$	0	< 0.39 (90% CL)	0.033 ± 0.006	< 1.45
$M_X = 200$	0	0.28 ± 0.19	0.022 ± 0.004	< 1.15
$M_X = 205$	0	0.46 ± 0.24	0.019 ± 0.004	< 1.02
$M_X = 210$	1	0.19 ± 0.13	< 0.01	< 1.25
$M_X = 215$	0	0.10 ± 0.10	< 0.01	< 0.903
$M_X = 220$	0	< 0.30 (90% CL)	< 0.01	< 1.24
$K_L \to \pi^0\pi^0\gamma\gamma$	0	1.09 ± 0.52	0.24 ± 0.03	< 16.9

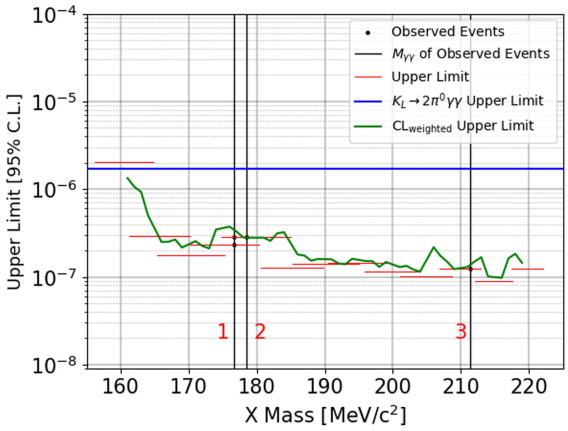


FIG. 5. 95% CL upper limits. The width of each discrete line shows the ROI for the respective analysis. The points correspond to the three unique observed events and their invariant mass.

masses between those studied in Table II. The CL_s is evaluated based on the signal acceptance of the integer test mass within each ROI. Each integer X mass is labeled by m, and the weighted CL_s is evaluated as

$$CL_{\text{weighted}}(m) = \frac{\sum_i CL_{s,i}(m) h_i}{\sum_i h_i}, \tag{6}$$

where h_i is the probability density function of the fitted Gaussian at the ith analysis mean. The signal branching ratio assumption that gives a $CL_{\text{weighted}} = 5\%$ is the 95% CL upper limit. The results are summarized in Fig. 5.

Conclusion and prospects—We have performed a search for $K_L \to \pi^0\pi^0 X$, where X decays to $\gamma\gamma$ promptly, and $K_L \to \pi^0\pi^0\gamma\gamma$ at the KOTO experiment using the data taken in 2021. The range of X mass studied was in the range 160–220 MeV/c^2, with better sensitivity farther from the pion mass. Three events were observed in the signal regions, with two events near an X mass of 177 MeV/c^2. This result led to a range of upper limits on the branching ratio, $\text{BR}(K_L \to \pi^0\pi^0 X) < (1-20) \times 10^{-7}$ at the 95% CL and may directly constrain models where ALP production from neutral three-body decays dominates the two-body modes [5]. No events were observed for the analysis of $K_L \to \pi^0\pi^0\gamma\gamma$, setting an upper limit on the branching ratio, $\text{BR}(K_L \to \pi^0\pi^0\gamma\gamma) < 1.69 \times 10^{-6}$, at the 95% CL.

Acknowledgments—We would like to express our gratitude to all members of the J-PARC Accelerator and Hadron Experimental Facility groups for their support. We also thank the KEK Computing Research Center for KEKCC and the National Institute of Informatics for SINET4. The high throughput simulation was performed with the aid of the University of Chicago Computational Institute and the Open Science Grid Consortium. This material is based upon work supported by the Ministry of Education, Culture, Sports, Science, and Technology (MEXT) of Japan and the Japan Society for the Promotion of Science (JSPS) under KAKENHI Grants No. JP16H06343 and No. JP21H04995 and through the Japan-U.S. Cooperative Research Program in High Energy Physics; the U.S. Department of Energy, Office of Science, Office of High Energy Physics, under Award No. DE-SC0009798; the National Science and Technology Council (NSTC) and Ministry of Education (MOE) in Taiwan, under Grants No. NSTC-108-2112-M-002-001, No. NSTC-109-2112-M-002-021, No. NSTC-110-2112-M-002-020, No. NSTC-111-2112-M-002-032, No. NSTC-114-2112-M-018-005-MY3, No. MOE-109L892105, and No. MOE-110L890205 through National Taiwan University; the National Research Foundation of Korea under Grants No. 2020R1A3B2079993, No. RS-2022-NR070836, and No. RS-2025-00556834.

Data availability—The data that support the findings of this article are not publicly available because they are owned by a third party and the terms of use prevent public distribution. The data are available from the authors upon reasonable request.

[1] D. Aloni, Y. Soreq, and M. Williams, Phys. Rev. Lett. **123**, 031803 (2019).
[2] J. Kumar, Phys. Rev. D **98**, 116009 (2018).
[3] M. Bauer, M. Neubert, S. Renner, M. Schnubel, and A. Thamm, Phys. Rev. Lett. **127**, 081803 (2021).
[4] M. Bauer, M. Neubert, S. Renner, M. Schnubel, and A. Thamm, J. High Energy Phys. 02 (2022) 056.
[5] R. Balkin, S. Gori, and C. Scherb, J. High Energy Phys. 02 (2026) 011.
[6] R. Balkin, S. Gori, D. J. Robinson, and C. Scherb, Phys. Rev. D **113**, 075034 (2026).
[7] Y. C. Tung, Y. B. Hsiung, M. L. Wu, K. F. Chen *et al.* (E391a Collaboration), Phys. Rev. Lett. **102**, 051802 (2009).
[8] R. Funck and J. Kambor, Nucl. Phys. **B396**, 53 (1993).
[9] Alavi-Harati *et al.* (KTeV Collaboration), Phys. Rev. Lett. **89**, 211801 (2002).
[10] E. Abouzaid *et al.* (KTeV Collaboration), Phys. Rev. Lett. **107**, 201803 (2011).
[11] A. J. Buras and E. Venturini, Acta Phys. Pol. B **53**, 6-A1 (2022).
[12] J. Ahn *et al.* (KOTO Collaboration), Phys. Rev. Lett. **134**, 081802 (2025).
[13] T. Shimogawa, Nucl. Instrum. Methods Phys. Res., Sect. A **623**, 585 (2010).
[14] K. Sato, Ph.D. thesis, Osaka University, 2015.
[15] K. Shiomi *et al.*, Nucl. Instrum. Methods Phys. Res., Sect. A **664**, 264 (2012).
[16] K. Sato *et al.*, Nucl. Instrum. Methods Phys. Res., Sect. A **982**, 164527 (2020).
[17] R. Murayama, M. Togawa *et al.*, Nucl. Instrum. Methods Phys. Res., Sect. A **953**, 163255 (2020).

[18] Y. Tajima *et al.*, Nucl. Instrum. Methods Phys. Res., Sect. A **592**, 261 (2008).
[19] D. Naito *et al.*, Prog. Theor. Exp. Phys. **2016**, 023C01 (2016).
[20] Y. Maeda *et al.*, Prog. Theor. Exp. Phys. **2015**, 063H01 (2015).
[21] C. Lin, Y. B. Hsiung, Y. W. Wah, Y. C. Tung, Y. T. Luo, and M. Bogdan, J. Phys. Conf. Ser. **1526**, 012034 (2020).
[22] Y.-C. Tung *et al.*, Nucl. Instrum. Methods Phys. Res., Sect. A **1059**, 169010 (2024).
[23] G. Cowan, K. Cranmer, E. Gross, and O. Vitells, Eur. Phys. J. C **71**, 1554 (2011).
[24] S. Agostinelli *et al.*, Nucl. Instrum. Methods Phys. Res., Sect. A **506**, 250 (2003).
[25] A. L. Read, J. Phys. G **28**, 2693 (2002).